Multiscale Structural Modulation of Anisotropic Graphene Framework for Polymer Composites Achieving Highly Efficient Thermal Energy Management

Wen Dai,[a,b] Le Lv,[a,b] Tengfei Ma,[c] Junfeng Ying,[a,b] Qingwei Yan,[a] Xue Tan,[a,b] Jingyao Gao,[a,b] Ke Yang,[a,b] Jinhong Yu,[a,b] Yagang Yao,[d] Rong Sun,[e] Yan Wang,[c] Nan Jiang,*[a,b] Ching-Ping Wong,[f] Qunji Xue [a,b] and Cheng-Te Lin*[a,b]

[a] *Key Laboratory of Marine Materials and Related Technologies, Zhejiang Key Laboratory of Marine Materials and Protective Technologies, Ningbo Institute of Materials Technology and Engineering (NIMTE), Chinese Academy of Sciences, Ningbo 315201, P.R. China*

[b] *Center of Materials Science and Optoelectronics Engineering, University of Chinese Academy of Sciences, Beijing 100049, P.R. China*

[c] *Department of Mechanical Engineering, University of Nevada, Reno, Reno, Nevada 89557, USA.*

[d] *National Laboratory of Solid State Microstructures, College of Engineering and Applied Sciences, Jiangsu Key Laboratory of Artificial Functional Materials, and Collaborative Innovation Center of Advanced Microstructures, Nanjing University, Nanjing 210093, China.*

[e] *Shenzhen Institutes of Advanced Technology, Chinese Academy of Sciences, Shenzhen 518055, China.*

[f] *School of Materials Science and Engineering, Georgia Institute of Technology, Atlanta, Georgia 30332, United States.*

ABSTRACT: Graphene is usually embedded into polymer matrices to develop thermally conductive composites, preferably in the form of an interconnected and anisotropic framework. Currently, the directional self-assembly of chemically exfoliated graphene sheets has been demonstrated as the most effective way to synthesis anisotropic graphene frameworks. However, achieving a thermal conductivity enhancement (TCE) over 1500% with per 1 vol% graphene content in polymer matrices remains a great challenge, resulting in the composites ever reported with a limited thermal conductivity, which is essentially because the spontaneous assembly process could just form an incompact contact of the graphene sheets, thereby generating a high junction thermal resistance. Here, a multiscale structural modulation strategy for reducing the junction thermal resistance between adjacent graphene sheets of the anisotropic graphene framework was demonstrated. The as-prepared graphene framework contributes to the polymer composites a record-high thermal conductivity of $56.8 - 62.4$ W m^{-1} K^{-1} with a similar level of graphene content (≈ 13.3 vol%), giving an ultra-high TCE per 1 vol% graphene over 2400%. Furthermore, the thermal energy management application of the composites as phase change materials for solar-thermal energy conversion and as thermal interface materials for electronic devices cooling are demonstrated. This finding provides a valuable guidance for designing high-performance thermally conductive composites and raises their possibility for the practical use in thermal energy storage and thermal management of electronics.

KEYWORDS: multiscale structural modulation, vertically aligned graphene, phase change composites, thermal interface materials, thermal energy management.

In recent decades, along with the rapid developments of electronic and energy technologies, a serious issue concerning thermal energy management has gradually emerged and is becoming of crucial importance for improving the efficiency of various devices.[1-3] For example, in semiconductor industry, the shrinking feature size and escalating power density of transistors and integrated circuit packaging promote a significant enhancement of the computing capability, but resulting in an increase of heat dissipation across the chip, board, and system levels.[4, 5] The accompanying interfacial heat transfer problem leads to an urgent demands for thermal interface materials (TIMs) with high thermal conductivity for removing excess thermal energy to guarantee the continuous and stable operation of the electronic device.[6-8] And in the field of thermal energy harvesting based on the phase-change technology, the low intrinsic thermal conductivity (< 0.5 W m^{-1} K^{-1}) of the phase-change materials (PCMs) is a long-standing bottleneck, which greatly limited the thermal charging/discharging rate, thus causing a low heat-utilization efficiency for diverse applications of PCMs, such as solar-thermal energy conversion, thermal management of batteries and thermal diodes.[9, 10] Therefore, addressing the thermal energy management issue including the extraction of detrimental heat and the efficient utilization of beneficial heat by developing advanced thermally conductive materials has become a necessity for the sustainable and stable development of the electronics and energy industries.

Graphene is a monolayer of covalently sp^2-hybridized carbon atoms in a honeycomb lattice, exhibiting an extremely high thermal conductivity over 5,000 W m^{-1} K^{-1}, which is more than 10 times that of copper.[11, 12] Such an excellent heat conduction performance has triggered considerable research interest in developing diverse graphene-based materials for meeting the ever-increasing thermal energy management requirement, including graphene papers as heat spreaders,[13-15] graphene

aerogels for solar thermal generation,[16, 17] graphene textiles for thermal camouflage,[18] and graphene/polymer composites.[19, 20] In particular, graphene/polymer composites, which were prepared by embedding graphene into polymer matrices, have been continuously spotlighted and implemented various applications in the electronics and energy field, due to the improved heat conductance, low density, excellent chemical stability and ease of processing.[21-23] Currently, the direct dispersion of chemically exfoliated graphene sheets in polymer matrices by a solution or melt-blending process is the most common way to prepare graphene/polymer composites.[24, 25] In this case, the critical issue is the intrinsically high contact thermal resistance between dispersed graphene sheets and polymer matrices, deriving from their poor interface based on weak van der Waals interaction, which greatly limits the thermal conductivity enhancement of the resultant composites.[20, 26] Generally, to achieve an efficient thermal percolation pathway, a high graphene content up to $20 - 30$ vol% in polymer matrix is required, but nonetheless, the currently reported thermal conductivity enhance (TCE) is mostly lower than 3,000%, resulting in an unsatisfactory thermal conductivity of $4 - 6$ W m^{-1}K^{-1}.[22, 27] TCE is calculated using the equation of TCE = $(\kappa - \kappa_m)/\kappa_m \times 100$ %, and increases with more graphene addition, where κ and κ_m are the thermal conductivity of composites and polymer matrix, respectively. To more effectively evaluate the thermal conductivity enhancement effect of the applied filler and explore the potential research value of the composites, the TCE per 1 vol% graphene addition named specific TCE is adopted.[22] To date, the reported specific TCE of the polymer matrices using the dispersed graphene as filler is almost less than 200%, inherently restricting the real thermally conductive applications of the corresponding composites.[25, 28-30]

Recently, three dimensional graphene frameworks composed of interconnected graphene sheets has emerged as an ideal reinforcement to develop thermally conductive polymer composite, due to

the formation of continuous thermal pathway of graphene-graphene for rapid phonon transport.[31-33] And more effective thermal conductivity enhancement can be achieved by the modulation of the graphene framework to form a highly ordered and anisotropic structure instead of random arrangement.[19, 34] It can be attributed to the fact that the thermal conductivity of graphene is highly anisotropic, having an excellent capability to transfer heat along the basal plane ($\approx$ 5,300 W m^{-1}K^{-1} in theory) but much poorer along its cross-plane direction (< 2 W m^{-1}K^{-1}).[35, 36] Current methods for the development of anisotropic graphene framework using graphene sheets, such as graphene oxide (GO), reduced GO (rGO) and graphite nanoplatelets (GNPs), can be typically divided into two approaches: the directional-freezing of rGO aqueous dispersion and self-assembly of GO liquid crystals.[37-40] The former was usually carried out based on an ice-templated assembly strategy, by which the graphene sheets can be spontaneously restacked on the edges of the unidirectional grown ice crystals to form an ordered arrangement.[41-43] After incorporating with polymer matrices, typically, the thermal conductivity of the composites along the preferred direction can be up to 2.13 W m^{-1}K^{-1} with a graphene content of 0.92 vol%, corresponding to the specific TCE of 1338%.[21] The anisotropic graphene framework can also be readily prepared utilizing the liquid crystals behavior of GO, which arises from their intrinsic shape anisotropy and mutual electrostatic-repulsion, leading to the directional self-assembly of GO with a long-range ordered structure in the aqueous dispersion.[44, 45] After a air-drying followed by a graphitization treatment at 2800 °C, Yu et al. embedded the as-prepared anisotropic framework into the epoxy, and obtained a currently record-high thermal conductivity of 35.5 W m^{-1}K^{-1} for the graphene/epoxy composites (19 vol%), giving a specific TCE up to 884% along the preferred direction.[46] Although the above strategies have achieved a significant thermal conductivity enhancement of the polymer by incorporating the anisotropic graphene

framework, the thermal resistance between the adjacent graphene sheets within those graphene framework is still fairly high. This is essentially because the graphene framework prepared through the currently most used spontaneous assembly method could just form an incompact contact between the adjacent graphene sheets with a low overlapping area of graphene-graphene.[22] Such a microscopic junction thermal resistance can ultimately contribute to the high total thermal resistance inside bulk composites, limiting the specific TCE mostly below about 1,500% for the anisotropic graphene framework/polymer composites ever reported.[9, 21, 46, 47] Therefore, the further interface optimization for reducing the junction thermal resistance between the adjacent graphene sheets within the anisotropic graphene framework is imperative to further improve the thermal conductivity of graphene-based polymer composites.

Herein, we report a dual-assembly strategy with a multiscale structural modulation process to construct anisotropic graphene framework, which has not only a highly oriented arrangement of graphene along the vertical direction, but also an intimate contact of the adjacent graphene sheets with a low junction thermal resistance. As a result, the dual-assembled graphene framework (DAGF) exhibited an excellent thermal conductivity enhancement effect on various polymer matrices, typically endowing the epoxy composites with a record-high through-plane thermal conductivity of 62.4 W m^{-1} K^{-1} with a similar level of graphene content ($\approx$ 13.3 vol%). This value achieved is equivalent to $\approx$ 325 times higher than that of neat epoxy, giving an ultra-high specific TCE over 2400%, significantly outperforming previously reported graphene/polymer composites. Additionally, in view of practical applications of thermal energy management including the efficient utilization of beneficial heat and the extraction of detrimental heat, we further incorporated the as-prepared DAGF with the polyethylene glycol (PEG) and the polydimethylsiloxane (PDMS). And the resultant

DAGF/PEG and the DAGF/PDMS composites demonstrated a superior performance using as phase change materials (PCMs) for solar-thermal energy conversion and as thermal interface materials (TIMs) for cooling electronic devices, respectively. Our finding provides insight for the construction of graphene-based thermally conductive composites, which may meet the ever-increasing thermal energy management issue of in electronics and energy field.
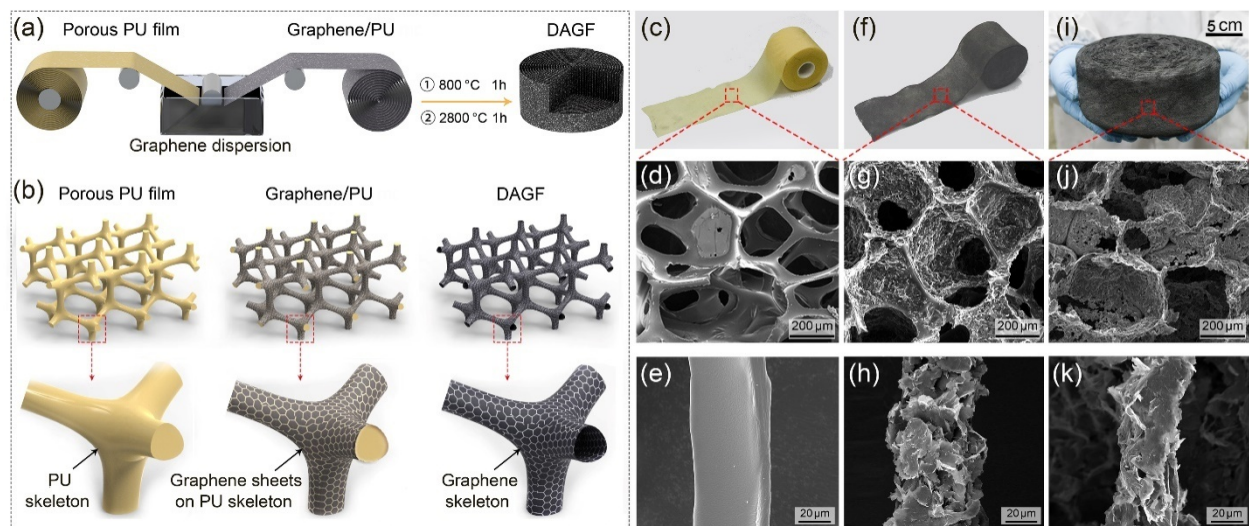
RESULTS AND DISCUSSION

Figure 1. Schematic illustrating the (a) fabrication process of the DAGF and (b) the corresponding structural change of each step based on the proposed dual-assembly method. Optical and SEM images of the (c – e) porous PU film, (f – h) graphene/PU and (i – k) DAGF, respectively.

Figure 1a illustrates our strategy for synthesizing the DAGF with the corresponding structural change of each step during the preparation process showing in **Figure 1**b. The detailed description of the overall procedures can be found in the Experimental Section. In brief, the graphene/polyurethane (graphene/PU) was prepared first through a dual-assembly method, which adopts a porous PU thin

film as the starting template to assemble graphene sheets on its skeletons using a solution immersion process, followed by a roll-to-roll step to continuously assemble the film into a large scale monolith using a self-developed roller equipment. As shown in **Figure 1**c–d, commercial PU film with the thickness of ≈ 500 μm has a continuous and interconnected macropore structure, whose cellular size is in the range of 200 – 400 μm, and in **Figure 1**e, the internal skeleton of the PU film presents a fairly smooth surface with its wire diameter of ≈ 40 μm. After the continuous immersion of PU film into the graphene/ethanol dispersion (10 mg/ml), the color of the film turned from yellow to black (**Figure 1**b and f), due to the uniform coating of graphene sheets onto the PU skeleton (**Figure 1**g). In **Figure 1**h, it can be observed that graphene sheets preferred to be face-to-face attached on the surface of the PU skeleton, due to the ultrathin nature of two-dimensional graphene sheets with a high aspect ratio (> 500) and the relatively strong adhesive between graphene sheets and the PU.[48] In the subsequent roll-to-roll process, the black film was continuously rolled up into a cylindrical monolith (graphene/PU), and its finished size was mainly depended on the length of the applied film. For example, a large-scaled graphene/PU with a diameter of ≈ 20 cm and thickness of ≈ 8 cm can be fabricated by continuously rolling up a 60 meter-long film. Finally, as shown in **Figure 1**i, the DAGF with the same dimension can be obtained by the pyrolysis of the graphene/PU at 800 °C (1h) to remove the PU template. And the quality of DAGF can be further improved by a post-thermal annealing at 2800 °C (1h) for repairing the structural defects and enlarging the domain size of the graphene, based on the Raman and XRD analysis shown in **Figure S1**. **Figure 1**j indicates that the resultant DAGF can still maintain the characteristic interconnected cellular structure with a slight contraction of the skeleton (**Figure 1**k) compared to the original morphology of starting PU film.
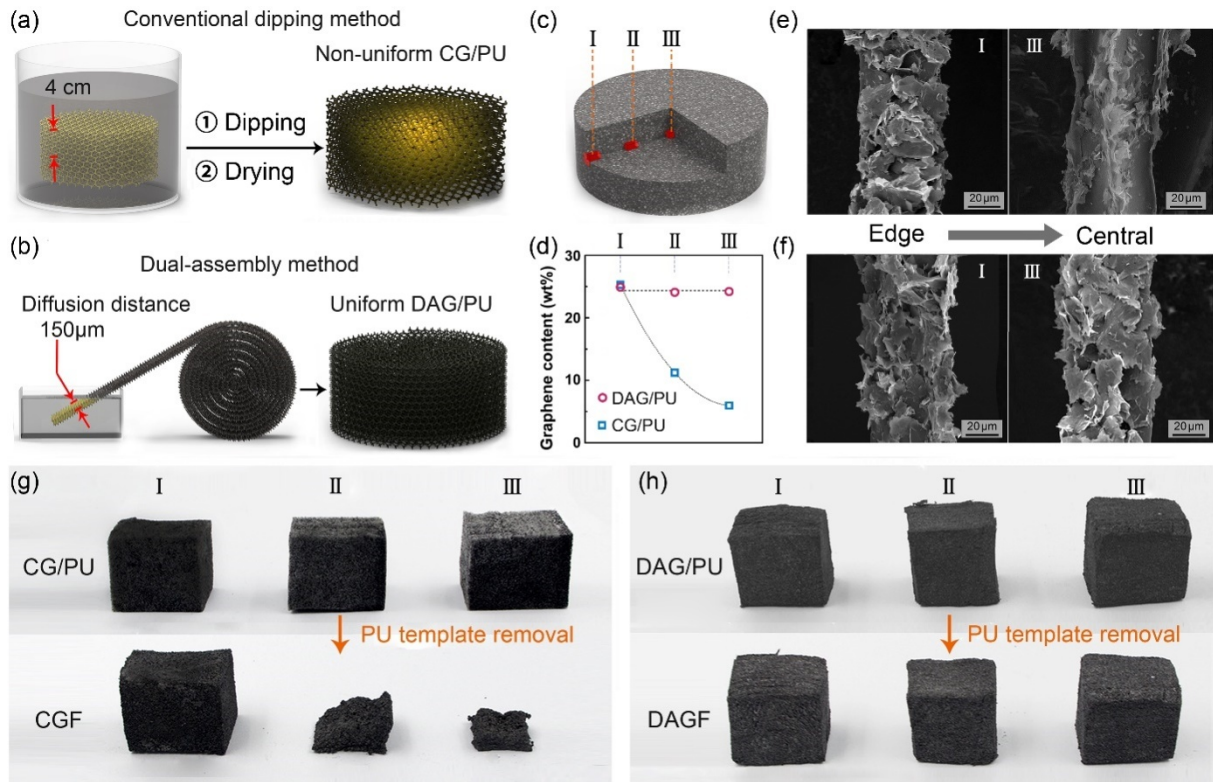
Figure 2. Schematic illustrating the incorporation of graphene sheets and the porous PU sponge using (a) conventional dipping method and (b) our proposed dual-assembly method to fabricate the graphene/PU. (b) Schematic illustrating three different sampling regions from edge to the central within graphene/PU. (c) The graphene content in the different regions of the two types of graphene/PU, with the corresponding SEM images showing in (e) and (f) for the case of CG/PU and DAG/PU, respectively. The photograph of selected graphene/PU cubies before and after the PU template removal for the case of (e) CG/PU and (f) DAG/PU.

Actually, the fabrication of interconnected graphene frameworks using porous PU sponge as the sacrifice template has been widely reported in previous works.[49-51] And the most common method was performed according to a "dipping and drying" process illustrated in **Figure 2**a, in which the bulk PU sponge was directly immersed into the graphene dispersion for coating graphene sheets on

its skeleton, followed by thermal annealing for the removal of organic template to obtain the graphene framework.[52] However, it is difficult for this conventional dipping method to achieve a large scale graphene framework while guaranteeing the homogeneity of the entire structure. It mainly because when a large scale PU sponge was simply immersed into the graphene dispersion, the graphene sheets attached at the outer surface of sponge would form a diffusion barrier layer to prevent the continuous penetration of dispersion toward central region, similar to filtration membrane, finally leading to the non-uniform assembly of graphene sheets after drying. For the case of our proposed dual-assembly strategy, the porous PU film with the thickness of 500 μm (**Figure S2**) was used as the starting template and immersed into the graphene dispersion, by which graphene sheets can diffuse from the normal direction of the applied PU film with a short diffusion distance of 250 μm. As illustrated in **Figure 2**a and b, when preparing a same size graphene framework shown in **Figure 1**i (Φ 20 × 8 cm^3), the diffusion distance of the dual-assembly method (250 μm) is almost 16 times shorter than that of the conventional dipping method (4 cm), leading to the ease of uniformly attaching the graphene sheets on all of the PU skeleton. The subsequent roll-to-roll step was carried out to post-assemble the as-prepared homogeneous graphene/PU film into a large scale graphene/PU monolith with uniformly distributed graphene sheets.

In order to intuitively demonstrate this point, the microscopic morphologies and graphene content at the different regions from the edge to the central of the dual-assembled graphene/PU (DAG/PU) monolith (Φ 20 × 8 cm^3) was investigated, with the three typical sampling regions illustrating in **Figure 2**c. For comparison, a controlled experiment was carried out on the same scale of conventional graphene/PU (CG/PU) prepared using the conventional "dipping and drying" method. Based on the thermogravimetric analysis (**Figure 2**d and **Figure S3**) and acquired SEM

images (**Figure 2**e), the three sampling regions in the DAG/PU exhibit a similar morphology with an approximate content of graphene sheets attaching on the PU skeleton surface, confirming the uniformly distribution of graphene sheets in the large scale graphene/PU. In sharp contrast, an obvious diminishing in the graphene content can be found from the edge to the central region for the case of CG/PU (**Figure 2**d, 2f and **Figure S3**). As a result, based on the distribution difference of graphene sheets within the two types of graphene/PU, the annealing of the three graphene/PU cubes (2 × 2 × 2 cm^3) cut out from the three sampling regions in DAG/PU and CG/PU exhibits fundamentally different result. In **Figure 2**g and h, DAGFs present nearly consistent shape compared to the original graphene/PU cubes, whereas a serious collapse of the CGFs can be found for the sampling regions away from the edge of the CG/PU monolith after the template removal, due to the lack of enough graphene sheets to support the structure. This result indicates that our proposed dual-assembly strategy is more feasible compared to the current commonly used "dipping and drying" method for the construction of nano-sized graphene sheets into homogeneous graphene framework with large scale.

The proposed dual-assembly strategy can not only efficiently construct a homogeneous graphene framework with large scale, but also manipulate the structural orientation of the resultant framework, based on the excellent flexibility and stretchability of the applied porous PU film. As shown in **Figure 3**a and b, the applied PU film can be easily stretched out to ≈ 3.4 times its original length, with the isotropic porous structure elongating into spindle-shaped structure for the stretched sample. According to this fascinating feature, a series of DAGFs (DAGF1 – DAGF5) were prepared by controlling the PU film with different stretch ratio in the roll-to-roll process, and the microstructure change of the resultant DAGFs were presented in **Figure 3**c–h. As shown in **Figure 3**c, the DAGF

prepared using the un-stretched PU porous film as the starting template (DAGF1) exhibits a fairly loose skeleton structure composed of quasi-isotropic arrangement of graphene sheets (**Figure 3**d and e). Based on this characteristic structure, the roll-up of a 1.6 meter-long film can finally achieve a cylindrical graphene framework with the diameter about 32 mm (**Figure 3**c). In sharp contrast, by rolling-up a 3.4-fold stretched film with the same original length, the resultant DAGF (DAGF5) presents an obviously lessened diameter of ≈ 15 mm (**Figure 3**f). And more interestingly, in comparison with the loose and quasi-isotropic porous structure of DAGF1 (**Figure 3**d and e), the DAGF5 has a more densely packed structure composed of highly ordered arrangement of graphene sheets toward the vertical direction, as shown in **Figure 3**g and h. We proposed that the microstructure change of the DAGFs from quasi-isotropic to obviously anisotropic with increasing stretch ratio of the PU film can be ascribed to the excellent stretchability of the applied film. In the continuous roll-to-roll step, when the elastic film under stretched state was rolled up into a cylindrical shape, the natural contraction behavior of the PU film provides a constant circumferential stress along the normal direction of the film. As schematically illustrated in **Figure 3**i, the generated circumferential stress can drive the quasi-isotropic graphene skeleton to transform into a highly ordered structure composed of vertically aligned graphene sheets. In addition, the density of the resultant DAGFs also presents an improvement with the increase of PU film stretch ratio, with the results showing in **Figure 3**j, in which the highest density of ≈ 270 mg cm^{-3} for the DAGF5 can be achieved at a stretch ratio of 340%. Note that the increasing trend of the density versus the stretch ratio was nearly linear, indicating a good controllability for modulating the density and the structural orientation of the graphene framework using our proposed dual-assembly strategy.
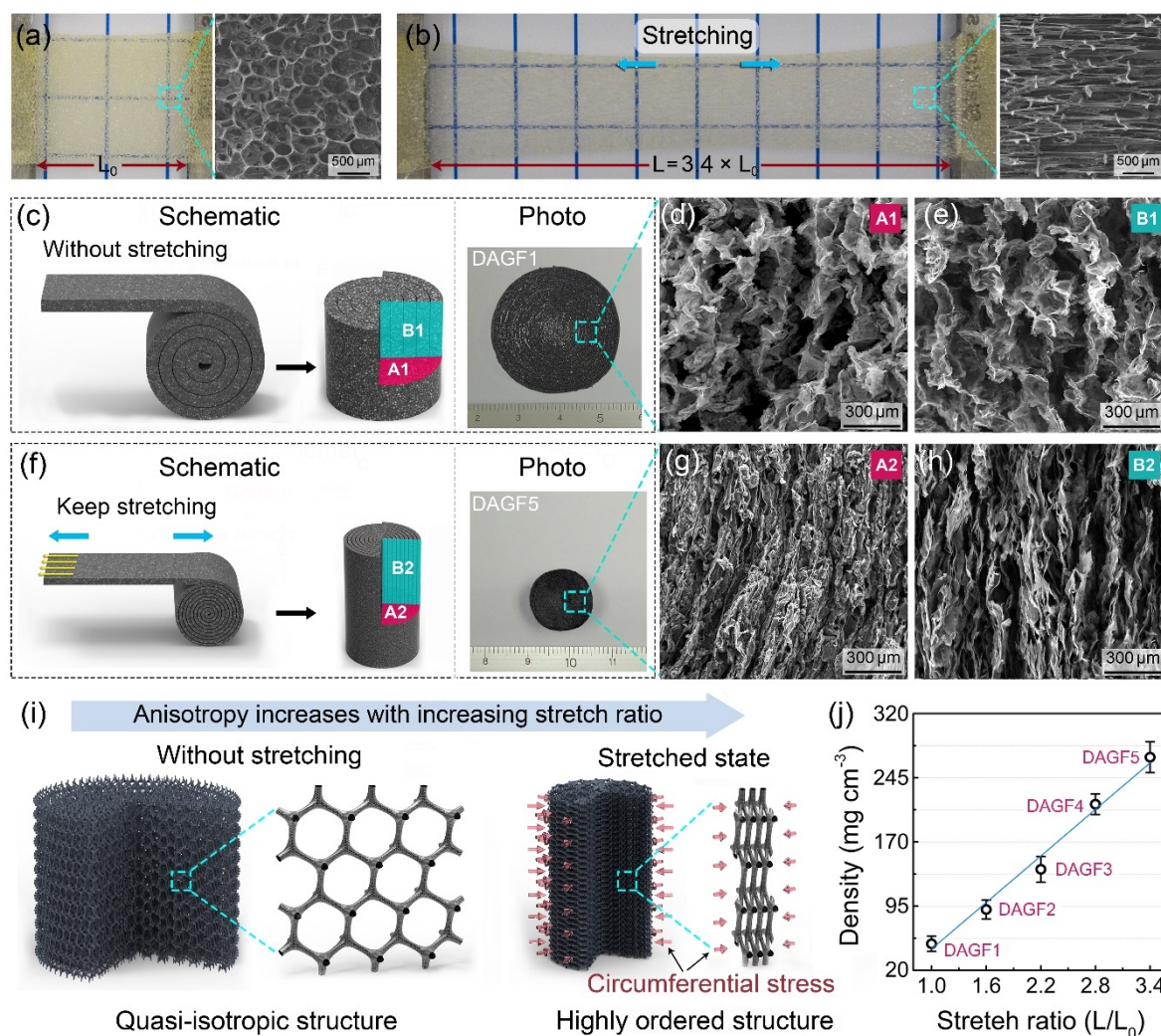
Figure 3. The photographs and the corresponding top-view SEM images of (a) un-stretched and (b) 3.4-fold stretched porous PU film. (c) Schematic, photograph, (d) top-view and (e) cross-sectional SEM images of DAGF prepared using the un-stretched PU porous film (DAGF1). (f) Schematic, photograph, (g) top-view and (h) cross-sectional SEM images of DAGF prepared through controlling the film stretch ratio of 340% (DAGF5). (i) Schematic illustrating the modulation of DAGF structure from quasi-isotropic to highly ordered arrangement with the increase of stretch ratio. (j) The densities of the resultant DAGFs as a function of stretch ratio.

Based on the characteristic interconnected structure composed of highly ordered graphene sheets,

the DAGF is expected to be a promising candidate as thermally conductive fillers embedded into polymer matrices to develop composites with improved thermal conductivity for the highly efficient thermal energy management. In order to confirm this point, the DAGF/epoxy (EP) composites were prepared, and the contribution of the DAGFs on the heat transfer capability of epoxy was studied. Epoxy was chosen because it is not only a widely utilized thermal management material in the electronic packaging field, but also the most commonly used polymer matrix for evaluating the heat transfer enhancing effect of the applied fillers in academia. In **Figure 4**a, a commonly used vacuum infiltration of epoxy, followed by thermal curing method was adopted to prepare the DAGF/EP composites, which were further cut into small pieces for the detection of their thermal conductivity along in-plane and through-plane direction (**Figure 4**b) using the laser flash technique. According to the five types of DAGFs with varying densities (**Figure 3**j), a group of DAGF/EPs (named as DAGF1/EP – DAGF5/EP) could be obtained, as shown in **Figure 4**c, in which the volume fraction of graphene in the DAGF/EPs was determined based on TGA analysis (**Figure S4**). In **Figure 4**d and **Table S1**, the composite with the lowest graphene content (DAGF1/EP, ≈ 2 vol%) exhibits in-plane ($\kappa_{/\!/}$) and through-plane ($\kappa_{\perp}$) thermal conductivities of 3.98 and 4.13 W m^{-1}K^{-1}, respectively, indicating an approximately isotropic heat transfer enhancing effect of low-density DAGF. When the DAGFs with higher density were incorporated, both $\kappa_{/\!/}$ and $\kappa_{\perp}$ of DAGF/EPs present a significant improvement as a function of graphene content. Interestingly, we noticed that the $\kappa_{/\!/}$ rises in an almost linear trend, whereas the increase of $\kappa_{\perp}$ is approximately exponential, leading to a monotonically increase of the thermal conductivity anisotropy ratio ($\kappa_{\perp}/\kappa_{/\!/}$) versus the graphene content, as shown in the inset of **Figure 4**d. As a result, by the combination of highest-density DAGF with epoxy, the $\kappa_{/\!/}$ and $\kappa_{\perp}$ of composite (DAGF5/EP, ≈ 13.3 vol%) can reach 24.8 and 62.4 W m^{-1}K^{-1},

respectively, corresponding to a thermal conductivity anisotropy ratio ($\kappa_\perp/\kappa_\parallel$) of 2.52. The changing trend from approximately isotropic to significantly anisotropic of thermal conductivity enhancement effect for the DAGF on the epoxy as the increase of graphene content can be attributed to the structural change of the applied DAGFs as discussed in **Figure 3**. The comparison of **Figure 3**e, h and **Figure 4**e indicates that, after incorporating with the epoxy, the DAGFs can maintain the characteristic structure within the matrix. As expected, the DAGF1/EP was embedded by a quasi-isotropic arrangement of graphene skeleton, which endows the composite with an approximately isotropic thermal conductivity. In sharp contrast, by incorporating the highest-density DAGF with highly anisotropic structure, the DAGF5/EP showed a preference for heat conduction along the through-plane direction. Particularly, based on the formation of highly efficient heat pathways toward the vertical direction composed of highly ordered graphene, the $\kappa_\perp$ achieved of DAGF5/EP (62.4 W m^{-1}K^{-1}) is over two order-of-magnitude higher than that of polymer (0.2 − 0.4 W m^{-1}K^{-1}), and outperforms that of many metals and ceramics.

Furthermore, we carried out a comparative test on through-plane heat transfer capacity between DAGF5/EP and tin (Sn) for directly demonstrating its ultra-high $\kappa_\perp$. In **Figure 4**f, DAGF5/EP and Sn ($\approx$ 56.7 W/mK) with the same size of 10 × 10 × 3 mm^3 were placed on a ceramic heater (60 W) for heating them at the same time from the room temperature. Besides, to precisely measure the time-dependent surface temperature of different materials using a commercial infrared (IR) camera, the top surface of the two samples was coated by a thin graphite layer ($\approx$ 5 μm) to ensure the same infrared emittance. As the results shown in **Figure 4**g and h, when the test started, the surface temperature of the DAGF5/EP rises faster as compared to that of Sn, leading to a significant temperature difference of 21 °C at 150 s, honestly determining the metal-level heat transfer capacity

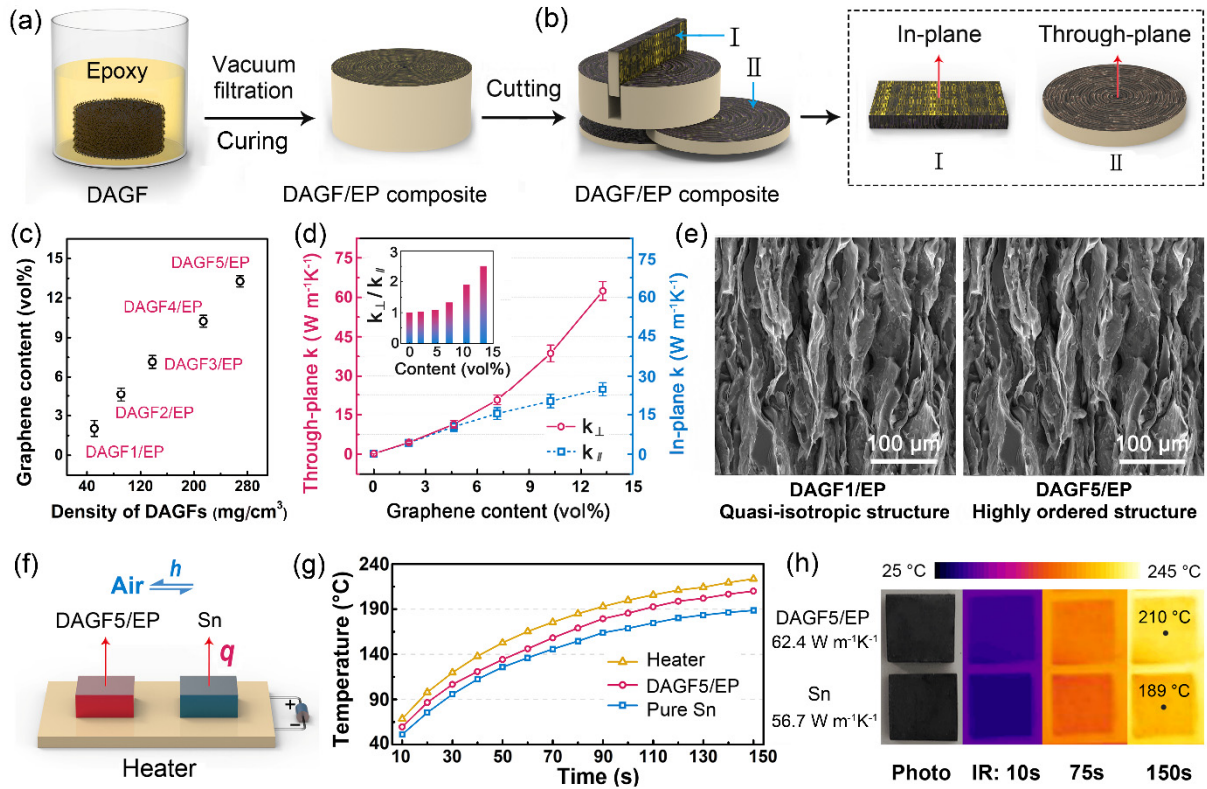of DAGF5/EP along the through-plane direction.

Figure 4. Scheme illustrating (a) the fabrication process of the DAGF/EP composites, and (b) the cutting of the sample into small pieces for the detection of thermal conductivities along in-plane and through-plane direction. (c) The volume fraction of graphene in the DAGF/EP composites versus the density of the DAGFs. (d) The in-plane ($\kappa_{//}$) and through-plane ($\kappa_{\perp}$) thermal conductivities of DAGF/EPs as a function of graphene content and the inset presenting the thermal conductivity anisotropy ratio ($\kappa_{\perp}/\kappa_{//}$). (e) The cross-sectional SEM images of DAGF1/EP and DAGF5/EP. (f) The test system configuration for demonstrating the through-plane heat transfer capacity. (g) Surface temperature evolution and (h) the corresponding IR images of DAGF5/EP and Sn versus heating time.

In order to comprehensively evaluate the heat transfer enhancing effect of our DAGFs on the polymer matrix, a comparison of thermal conductivity enhancement (TCE) between our DAGF/EPs and reported graphene/polymer composites was exhibited in **Figure 5**a and **Table S2**. The $\kappa_\parallel$ enhancement of DAGF/EPs presents a relatively consistent rising pattern as compared to the general trends of the currently reported results. However, it is interesting to note that the TCE of $\kappa_\perp$ shows an accelerated growth rate versus the graphene content, and begins to significantly outperform that of the latest reports when the graphene content exceeds about 10 vol%. To understand such an extraordinary $\kappa_\perp$ enhancement of DAGF/EPs, our experimental $\kappa_\perp$ was matched using a heat conduction model according to the metal foam theory, which takes the foam skeleton as the research object, and combines the κ_{skeleton} and the κ_{EP} through a rule of mixtures:[19, 22, 33]

$$k_\perp = \left\langle \cos^2 q \right\rangle f k_{\text{skeleton}} + \left(1 - f\right) k_{\text{EP}} \qquad (1)$$

where κ_{EP} is the thermal conductivity of the epoxy matrix; κ_{skeleton} is the solid thermal conductivity of an individual graphene skeleton of DAGFs; f is the volume fraction of graphene; θ is the angle between the graphene skeleton and the direction of heat transfer, and the angle bracket indicates the averaging value over all graphene skeleton. The detailed calculation and analysis can be seen in the Supporting Information (**Section S1**). As the results shown in **Figure 5**b, when the value of κ_{skeleton} was taken as 560 W m^{-1} K^{-1}, the predicted results of Equation (1) can well fit the first three points (f < 7.2 vol%) of our experimental data, whereas underestimate the $\kappa_\perp$ of the last two points, which can be matched by assigning a higher κ_{skeleton} of 770 and 950 W m^{-1} K^{-1} for Equation (1), respectively. Based on the correlation between the graphene content in DAGF/EP composites and the density of the applied DAGFs (**Figure 4**c), it is reasonable to assume that there should exist some mechanisms, which contribute to the higher-density DAGF having a superior heat conduction capability of the
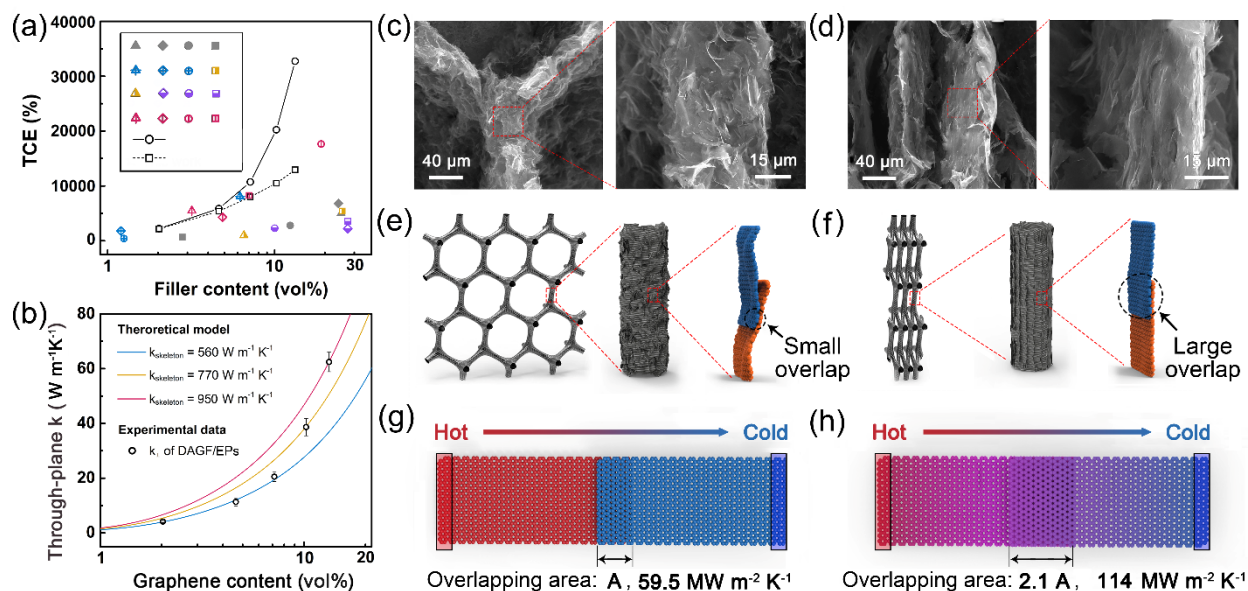
individual graphene skeleton.

Figure 5. (a) Comparison of thermal conductivity enhancement (TCE) of our DAGF/EP composites with reported graphene/polymer composites. [19, 20, 22, 24, 27-29, 31, 33, 46, 53-58] (b) Fitting of the experimental $\kappa_\perp$ of DAGF/EP composites based on the foam theory. (c – d) The morphologies and (e – f) scheme illustrating the rearrangement of DAGF including the graphene skeleton and the graphene sheets during the dual-assembly process. (c, e) and (d, f) show the cases of low-density DAGF (DAGF1) and high-density DAGF (DAGF5), respectively. The calculated junction thermal conductance of adjacent graphene sheets with (g) small and (h) large overlapping area based on the NEMD simulation. The arrow shows the direction of the heat flux.

Figure 5c and d show the comparative morphologies of the graphene skeleton within the DAGF1 (low density) and DAGF5 (high density), respectively. It is obvious that, different from the rough skeleton composed of the loosely stacked graphene sheets for DAGF1, the skeleton surface of

DAGF5 is fairly smooth with a dense stacking of graphene sheets, indicating a highly ordered arrangement along the direction of the skeleton. Accordingly, we proposed that the dual-assembly strategy with a continuous stress-induced orientation process can not only manipulate the arrangement of the graphene skeleton leading to the formation of highly ordered structure, but also further optimize the stacking order of the graphene sheets with increased overlapping area, as schematically illustrated in **Figure 5**e and f. This effect is similar to the rearrangement of graphene sheets within the graphene paper toward the horizontal direction by applying a vertical compression.[14] Based on the construction of anisotropic graphene framework using this multiscale structural modulation, the graphene skeleton of the higher-density DAGF has a closer contact of the adjacent graphene sheets with a larger overlapping area of graphene-graphene along the skeleton direction, thus leading to the direct improvement of the intrinsic $\kappa_{skeleton}$ as the increase of the density.

In order to in-depth study the quantitative relationship between the overlapping area of the adjacent graphene sheets and the thermal conductivity of the graphene skeleton for different dense DAGFs, a nonlinear model proposed by Foygel et al. was applied to analyze the $\kappa_\perp$ of the DAGF1/EP (low-density DAGF) and DAGF5/EP (high density DAGF), respectively.[59-61] As the thermal conductivity model given by Equation (2), the graphene sheets were chosen as the research object, and the contact resistance (R) and overlapping area (S) of adjacent graphene sheets can be estimated using the Equation (3) and (4):

$$k_\perp - k_{EP} = k_0 \left(\frac{f - f_c}{1 - f_c} \right)^t \qquad (2)$$

$$R = \frac{1}{k_0 L (f_c)^t} \qquad (3)$$

$$S = \frac{R_{\text{contanct}}}{R} = R_{\text{contanct}} \kappa_0 L(f_c)^{\tau} \qquad (4)$$

where $\kappa_\perp$ is the through-plane thermal conductivity of the composites versus the volume fraction (f); κ_{EP} is the thermal conductivity of epoxy matrix; κ_0 a preexponential factor ratio related to the contribution of graphene sheets; f_c is the critical volume fraction of graphene sheets and τ is a conductivity exponent; L is the plate size of the graphene sheets (≈ 5.4 µm); R_{contanct} is the interfacial thermal resistance of the overlapped graphene sheets based on the van der Waals (VdW) interaction, and therefore the R_{contanct} for the cases of DAGF1/EP and DAGF5/EP is the same, ideally, at the order of magnitude level of 10^{-9} K m^2 W^{-1}.[23] Based on the experimental $\kappa_\perp$ of DAGF1/EP and DAGF5/EP, as well as the corresponding change trend predicted using the Equation (1), the values of κ_0, τ and f_c for the two cases can be calculated, as listed in **Table S3**. Then according to the Equation (3), we obtained that the overlapping area of adjacent graphene sheets for the case of DAGF5/EP (9.56 $\times$ 10^{-14} m^2) is ≈ 2.1 times as high as that of DAGF1/EP (4.57 $\times$ 10^{-14} m^2). Moreover, based on the result of non-equilibrium molecular dynamics (NEMD) simulation (**Figure 5** g–h and **Figure S5**), we demonstrate that a 2.1-times enhancement of the overlapping area for adjacent graphene sheets can improve the junction thermal conductance along the basal plane direction by 92% (DAGF1/EP: 59.5 MW m^{-2} K^{-1}, DAGF5/EP: 114 MW m^{-2} K^{-1}). The detailed calculation and analysis of the Foygel model and the NEMD simulation can be found in the Supporting Information (**Section S2** and **Figure S5**). And the results confirm superior κ_{skeleton} of an individual graphene skeleton for the higher-density DAGFs, and provide fundamental evidence to explain the extraordinary $\kappa_\perp$ enhancement of DAGF/EP with the increase of the graphene content. As a result, the $\kappa_\perp$ enhancement of the corresponding DAGF/EP can be as high as 325 times that of neat epoxy at the

graphene content of 13.3 vol%. To the best of our knowledge, this $\kappa_\perp$ enhancement achieved is the highest value ever reported for graphene framework/polymer composites, and gives a remarkably high specific TCE (TCE per 1 vol% graphene content) over 2400%, significantly outperforming previously reported graphene/polymer composites.
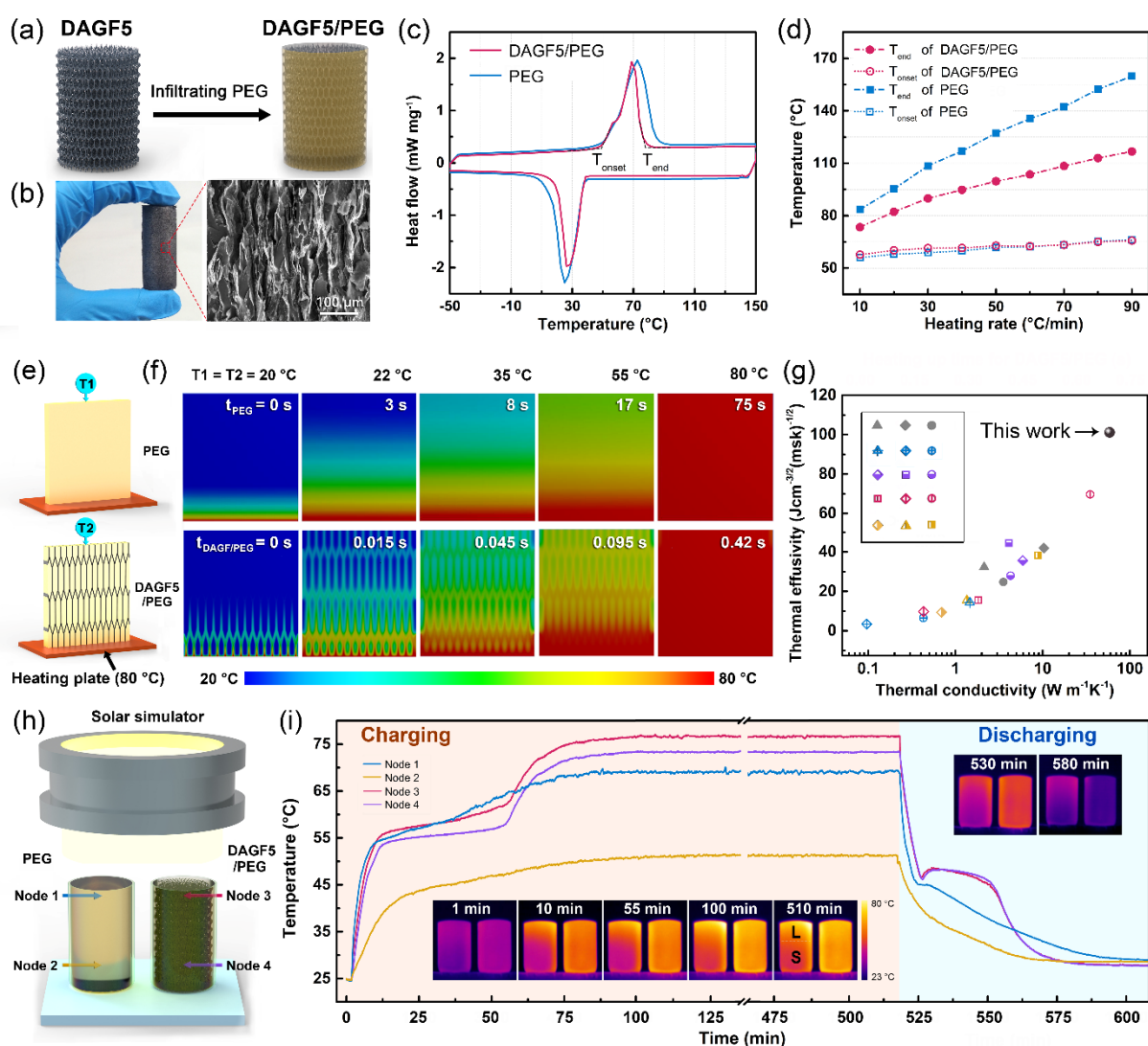

Figure 6. (a) Schematic illustrating the fabrication process of the DAGF5/PEG with the correspondingly photograph and cross-sectional SEM image showing in (b). (c) DSC heating and cooling scan curves for pure PEG and DAGF5/PEG with the heating rate of 10 $^\circ$C/min. (d) The T_{onset} and T_{end} of PEG and DAGF5/PEG versus the DSC heating rate. (e) Schematic of the ANSYS

simulation models and (f) the calculated transient temperature distribution for PEG and DAGF5/PEG. The temperature of the heating plate is maintained at 80 °C. (g) A comparison of the thermal conductivity and the thermal effusivity of our DAGF5/PEG and with the reported carbon-based phase-change composites.[9, 23, 32, 33, 53, 62-71] (h) Schematic illustrating the solar-thermal energy conversion measurement. (i) Temperature evolution curves for PEG and DAGF5/PEG under stimulant solar irradiation. The insets show the infrared images of the two samples during the charging and discharging process.

Efficient thermal energy harvesting using phase change materials (PCMs) has enormous potential for cost-effective energy storage and waste heat recovery.[10] However, the low intrinsic thermal conductivity of PCMs (< 0.5 W m^{-1} K^{-1}) resulting in a limited speed for the energy conversion is an everlasting bottleneck, causing a low efficiency for energy charging/discharging.[9] There have been numerous studies indicated that the incorporation of PCMs with three dimensional graphene frameworks, which severed as the continuous heat pathways within the matrices, is a feasible solution to develop highly thermally conductive PCMs for solving this difficult problem.[33, 53, 67] Hereby, based on the excellent performance of our DAGF in enhancing the thermal conductivity of polymer matrix, we embedded the polyethylene glycol (PEG, a sort of PCMs, 0.29 W m^{-1} K^{-1}) by the as-prepared DAGF5 using a conventional infiltration method (**Figure 6**a) and named the resultant composite as DAGF5/PEG. In **Figure 6**b, the obtained DAGF5/PEG composite with a diameter of 2 cm and a height of 5 cm presents a highly ordered microstructure composed of vertically aligned graphene sheets, in agreement with that of DAGF5/EP (**Figure 4**e), by which the DAGF5/PEG has a ultra-high $\kappa_\perp$ of 58.6 ± 2.2 W m^{-1}K^{-1} with ≈ 13.3 vol% graphene addition.

The differential scanning calorimetry (DSC) curves (**Figure 6**c) indicate that the calculated phase transition enthalpy (ΔH_m) of DAGF5/PEG is 139.7 J/g, which is about 78% that of neat PEG (179.2 J/g), attributing that the additional graphene component did not undergo a phase change. Besides, as shown in **Figure 6**c–d and **Figure S6**, the onset melting temperature (T_onset) of DAGF5/PEG is approximately the same as that of neat PEG, when the DSC heating rate was changed from 10 to 90 °C min^{-1}, suggesting that the embedding of graphene into PEG has no effect on its normal solid−liquid phase transition. But interestingly, in sharp contrast to the T_onset, the T_end (end melting temperature) of DAGF5/PEG (73.4 °C) presents a significant decrease of about 10 °C compared to that of PEG (83.6 °C) at the heating rate of 10 °C/min, and this temperature difference (ΔT_end) is further raised to 43 °C, as the heating rate up to 90 °C/min. We proposed that the faster phase-change speed of DAGF5/PEG compared to that of PEG can be attributed to its superior thermal conductivity (DAGF/PEG: 58.6 W m^{-1}K^{-1}, PEG: 0.2 W m^{-1}K^{-1}), substantially deriving from the highly ordered graphene sheets acted as the continuous heat channels within the PEG matrix.

Accordingly, a finite element modeling (FEM) using a commercial computational fluid dynamics software (ANSYS) is implemented to simulate the transient thermal response of neat PEG and DAGF5/PEG, for mimicking the DSC heating process. The simulation model of the two samples was shown in **Figure 6**e, in which the initial system temperature is 20 °C, and heating plate is maintained at 80 °C on the bottom side of the two modules, leading to the formation of one-dimensional heat conduction through the PEG and DAGF5/PEG. T1 and T2 are the temperature measurement points located at the top side of the PEG and DAGF5/PEG modules, respectively. More details about the simulations can be seen in the Supporting Information (**Figure S7**). As the calculated transient temperature distribution shown in **Figure 6**f, when the top side of the two

modules achieving a same temperature rise of 2 °C (T1 = T2 = 22 °C), the thermal response time of PEG and DAGF5/PEG is 3 s and 0.015 s, respectively, indicating that the embedding of DAGF5 can increase heat transfer rate by about a factor of 200 compared to that of neat PEG. As a result, in **Figure6**f and **Figure S7**e–f, the time needed to reach the equivalence point (T1 = T2 = 80 °C) for DAGF5/PEG module is only 0.45 s, which is more than two order of magnitude lower than that PEG (75 s). This simulation results directly demonstrate that the high thermal conductivity of DAGF5/PEG is a crucial factor to achieve a faster phase transition speed than that of neat PEG, leading to its significantly shortening of phase transition delay time during the DSC heating process. For PCMs, the thermal effusivity ($e = \sqrt{\kappa\, r\, \Delta H_m}$) can be used to evaluate their ability to exchange thermal energy with its surroundings, where κ, ρ, and ΔH_m are the thermal conductivity, density and phase change enthalpy of the PCMs, respectively.[63] As shown in **Figure 6**g and **Table S4**, based on the superior thermal conductivity of 58.6 W m^{-1}K^{-1}, contributing to an ultra-fast phase-change speed, our DAGF/PEG exhibit a record-high thermal effusivity as compared to the currently reported carbon-based phase-change composites.

In view of the practical application of thermal energy storage and management, DAGF5/PEG could be employed as a solar-thermal energy conversion materials, which work by the transformation of the absorbed solar energy at the surface into the thermal energy through a phase transition of the applied PCMs. The solar-thermal conversion performance test for neat PEG and DAGF5/PEG are illustrated in **Figure 6**h, in which a xenon lamp was applied as the solar simulator with an intensity of 1.5 sun, and the two samples in quartz crucibles have the same diameter of 2 cm and height of 3 cm. To record the real-time temperature change and temperature gradient of the test specimen, four thermocouples were inserted into the top and the bottom positions of the two samples (Node 1, 2 for

PEG and Node 3, 4 for DAGF5/PEG), respectively, and the total temperature profile evolution was captured using a calibrated infrared camera. More details about the light-to-thermal energy conversion measurement can be seen in the Supporting Information (**Figure S8**). In **Figure 6**i, when the neat PEG and DAGF5/PEG were solar-heated from the top surface, the temperature of the both increases over time. And in the steady state (100 – 510 min) during the charging process, the recorded temperature at the top and the bottom position of PEG is 69.1 °C (Node 1) and 51.3 °C (Node 2), respectively. It suggests that the PEG cannot completely accomplish a phase change (liquid/solid ratio, L/S ≈ 36 : 64) after 500 min of illumination, as shown in the IR images in the inset of in **Figure 6**i. This low efficiency of solar energy storage can be attributed to the intrinsic low thermal conductivity of PEG (0.29 W m^{-1}K^{-1}), which prevents the rapid spreading of absorbed heat energy from the top surface into the interior of the sample, showing a large temperature gradient of 8.9 °C/cm through the height direction the sample. In sharp contrast to the neat PEG, after the DAGF5/PEG being illuminated for nearly 55 min, the phase transition of the entire sample can be accomplished with the final steady-state temperature of 76.2 °C (Node 3) and 73.4 °C (Node 4) for the top and the bottom position, respectively. And at the steady-state of the charging process, the temperature gradient through the DAGF5/PEG is as low as 1.4 °C/cm, which demonstrates a fast heat transfer from the surface into the interior of the material, due to the super-efficient heat propagation along the thermally conductive graphene skeleton. During the heat discharging process without the light source, the temperature of the DAGF5/PEG is always higher than that of the PEG, and unlike the gradual decrease of the temperature of the PEG, the DAGF5/PEG presents a temperature plateau (46.5 – 48.5 °C) between 530 and 550 min. It suggests that the heat energy release for DAGF5/PEG can be maintained at a relatively high quality level in a wide range of

cooling time. Besides, different from the large temperature difference between the top and bottom of PEG, the temperature gradient through the DAGF/PEG is approaching to zero during the entire heat discharging process, indicating the superior heat discharging efficiency of DAGF5/PEG compared to that of PEG. The more excellent light-to-thermal energy conversion capability of DAGF/PEG compared to that of PEG during the charging and discharging process demonstrates the great potential for fast-charging/discharging solar-thermal energy conversion via the incorporation of the thermally conductive DAGF with the conventional phase change materials.
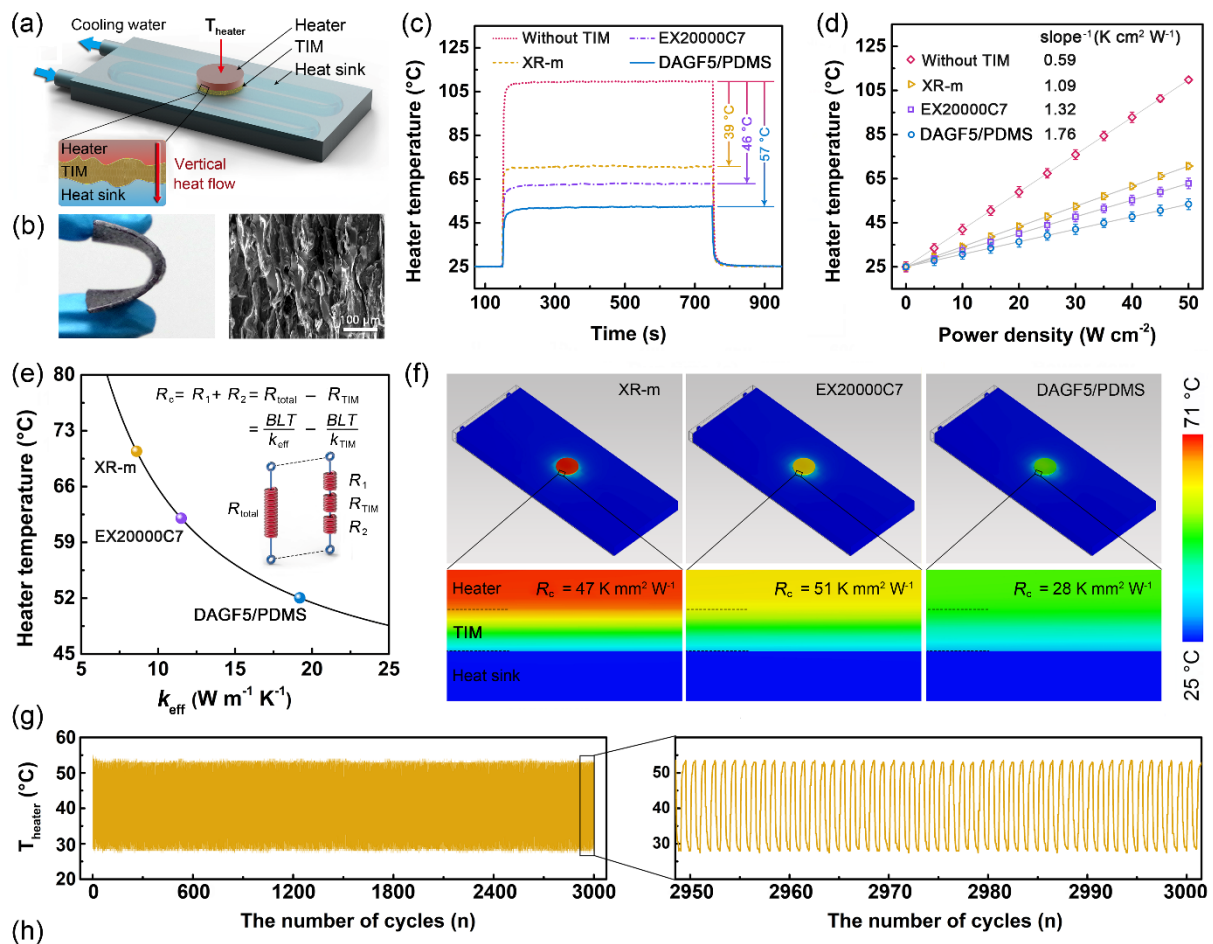

Figure 7. (a) Schematic configuration of TIM performance test system and the heat flow diffusion path along the vertical direction. (b) The photograph and the cross-sectional SEM image of the

The heater temperature evolution versus (c) the running time at the power density of 50 W cm^{-2} and (d) various power density after heating for 700 s. (e) The simulated effective thermal conductivity (κ_{eff}) of the applied TIM based on the heater temperature shown in (c). (f) The comparative heat dissipation capability according to the simulation results. (g) Thermal shock stability in cyclic heating/cooling tests and (h) thermal durability in a long-term TIM performance test (7 days) using DAGF5/PDMS as TIM.

In addition to as thermally conductive fillers incorporated with PCMs for the energy harvesting applications, the excellent capability of our DAGF in improving the $\kappa_{\perp}$ of polymer matrix can also endow the composites with considerable potential for use as high-performance thermal interface materials (TIMs). This is because TIMs are applied to bridge the heat generating electronic components (heater) and the heat sink for dissipating excess heat along the vertical direction, thus expecting to have a high $\kappa_{\perp}$ for maximizing the heat energy transfer efficiency,[72, 73] as schematic illustrating in **Figure 7**a. Therefore, we embedded the as-prepared DAGF5 into polydimethylsiloxane (PDMS, the most common matrix of TIMs, 0.18 W m^{-1} K^{-1}), and for the TIM applications, the resultant DAGF5/PDMS was cut into a thin pad with excellent bendability. In **Figure 7**b, the cross-sectional SEM image of the composite exhibited a vertically aligned graphene architecture inside the PDMS matrix, contributing to the composite with a superior $\kappa_{\perp}$ of 60.2 ± 2.5 W/mK ($\approx$ 13.3 vol%), which is much higher than that of current state-of-the-art commercial TIM (10 – 35 W m^{-1} K^{-1}).

In order to investigate the practical cooling performance of the as-prepared DAGF5/PDMS, a TIM performance test apparatus was built to simulate the actual heat transfer behavior of the

electronic devices. In **Figure 7**a, a circular DAGF5/PDMS with the diameter of 15 mm and the bond line thickness (*BLT*) of 800 μm was placed between the heater and heat sink at a packaging pressure of 75 psi. For comparison, the identical test for two types of commercial TIMs with the same size and packaging pressure were carried out, including a ceramic particle reinforced thermal pad ($\approx$ 17 W m^{-1} K^{-1}, Fujipoly XR-m, Japan) and a vertically aligned carbon fiber based thermal pad ($\approx$ 35 W m^{-1} K^{-1}, Dexerials EX20000C7, Japan). As far as we know, both of them are the state-of-the-art commercial products with the highest thermal conductivity in their respective fields. When the test system was started, a water cooling system was employed to keep the heat sink temperature constant at 25 °C, and the real-time temperature evolution of the heater (T_{heater}) was monitored using a calibrated thermocouple. As the results shown in **Figure 7**c, compared to the case of without TIM, an obvious cooling effect can be found by bridging the heater (50 W cm^{-2}) and the heat sink with TIMs. Noticeably, the cooling performance for DAGF5/PDMS with the heater temperature drop of 57 °C is substantially greater than that of XR-m (39 °C) and EX20000C7 (46 °C) thermal pads. In **Figure 6**d, according to the linear increase of the heater temperature versus the applied power density, the equivalent heat-transfer coefficients (equal to the reciprocal of the slope[74]) for the three TIMs can be calculated with the value of 1.76, 1.32 and 1.09 K cm^2 W^{-1}, assigned to the DAGF5/PDMS, EX20000C7 and XR-m thermal pads, respectively. This result indicates that the system cooling efficiency using DAGF/PDMS as TIM achieves 61% and 33% enhancement compared to that of the XR-m and EX20000C7 thermal pads, respectively.

A commercial flow solver (IcePak) was then adopted for the in-depth analysis of our test system at the power density of 50 W cm^{-2} (**Figure S9**a), and the effective thermal conductivity (κ_{eff}) of the three TIMs was calculated based on the steady-state heater temperature shown in **Figure 7**c. As the

simulated result shown in **Figure 7**e and **Figure S9**b–d, the κ_{eff} value of DAGF5/PDMS reaches up to 18.6 W m^{-1} K^{-1}, which is $\approx$ 2.2 times and $\approx$ 1.7 times as high as that of XR-m (8.5 W m^{-1} K^{-1}) and EX20000C7 (10.9 W m^{-1} K^{-1}) thermal pads, respectively. Besides, based on the equation: $R_{\mathrm{c}} = BLT/\kappa_{\mathrm{eff}} - BLT/\kappa_{\mathrm{TIM}}$, we calculated that our DAGF5/PDMS has a lower thermal contact resistance (two sides) of 28 K mm^{2} W^{-1} compared to that of current state-of-the-art commercial thermal pads (XR-m: 47 K mm^{2} W^{-1}, EX20000C7: 51 K mm^{2} W^{-1}). The details can be seen in the Supporting Information (**Table S5**), where the BLT and the κ_{TIM} are the thickness in packaging state and the through-plane thermal conductivity of the applied TIMs, respectively. The lower contact thermal resistance of our DAGF5/PDMS can be attributed to its lower filler volume fraction ($\approx$ 13.3 vol%) compared to that of the commercial thermal pads (50 – 70 vol%), leading to more soft matrix material directly in contact with the rough surface of the heater/heat sink with a better gap-filling. As a result, combining the dramatically higher through-plane thermal conductivity and the relatively lower contact thermal resistance, the simulated temperature profiles shown in **Figure 7**f demonstrate the excellent heat dissipation capability of our DAGF5/PDMS for TIM application.

Additionally, a cyclic thermal shock test using DAGF5/PDMS as TIM was carried out alternatively switching the power density between 5 and 50 W cm^{-2}. The measurement result in **Figure 7**g indicates an extremely steady performance in thermal energy removal of our DAGF5/PDMS during continuous heating/cooling impact for 3000 times. **Figure 7**h presents the result of a long-term TIM performance examination of DAGF5/PDMS by the continuously running the test apparatus (**Figure 7**a) at 50 W cm^{-2} for 7 days in a real environment, and the temperature of the heater (T_{heater}) and the ambient (T_{ambient}) were captured using thermocouple. The T_{heater} showed a fluctuated variation over time, attributing to the ever-changing T_{ambient}, which was vulnerable to the

large temperature difference between day and night, as well as the changes in the weather during the testing period. Despite that, the temperature difference between the heater and the ambient (T_{heater} - $T_{ambient}$) can remain almost unchanged during the whole test period, indicating an excellent long-term thermal durability of DAGF5/PDMS as TIM. The comparative TIM performance test suggests that by the incorporation of DAGF5 with soft PDMS matrix, the obtained composites can be a very promising candidate to replace the state-of-the-art commercial thermal pad for dealing with the ever-increasing heat dissipation requirement of next-generation advanced electronic devices.

CONCLUSIONS

In summary, we developed a highly ordered graphene framework with an intimate contact of its internal adjacent graphene sheets to achieve a superior specific TCE for polymer composites by a dual-assembly strategy. The key point of this strategy is the utilization of a stretchable porous PU thin film as the starting template to assemble graphene sheets on its skeletons, followed by a continuous roll-to-roll process to obtain a large scale graphene/PU monolith, which can be further thermally annealed to finally achieve the dual-assemble graphene framework (DAGF). Based on the natural contraction behavior of the elastic PU film providing a circumferential stress, the density and structural orientation of the DAGF can be facilely modulated by controlling the stretch ratio of the PU film in the roll-to-roll step. Besides, we demonstrated that the continuous stress-induced orientation effect in the dual-assembly process can not only manipulate the arrangement of the graphene skeleton leading to the formation of highly ordered architecture, but also further optimize the stacking order and overlapping area of the adjacent graphene sheets. As a result, by using a 3.4-fold stretched film as the starting materials, the resultant graphene framework (DAGF5)

exhibited an overlapping area enhancement of ≈ 2.1 times that of the un-stretched case, improving the thermal conductance of the overlapped graphene junction by 92% based on the NEMD simulation. Based on this multiscale structural modulation strategy leading to the resultant graphene framework combining the highly ordered architecture and a low junction thermal resistance, the as-prepared DAGF5 exhibited superior performance in improving the thermal conductivity of polymer, dramatically enhancing the $\kappa_\perp$ of epoxy by ≈ 325 times (62.4 W m^{-1} K^{-1}). To the best of our knowledge, this value achieved is the currently highest value for the graphene framework/polymer composite, and gives a ultra-high specific TCE over 2400%. Additionally, given the practical applications thermal energy management, the preparation and the performance study of the DAGF5/PEG and DAGF5/PDMS composites were simultaneously reported in this work. We demonstrated that the DAGF5/PEG as PCMs achieved an increased heat transfer rate by ≈ 200 times that the neat PEG in the solar-thermal energy conversion, and the DAGF5/PDMS performed excellently in application as TIM with the cooling performance enhancing by 33 − 61% compared to that of state-of-the-art commercial TIMs. The present work provides insights for the construction of graphene-based thermally conductive composites, which may satisfy the thermal energy management requirements arriving from the rapid developments of electronic and energy technologies. Furthermore, the proposed dual-assembly strategy is simple and versatile, which is not limited to graphene sheets but can also be applied toward the assembly and design of the other two-dimensional nanomaterials (boron nitride nanosheets, MXenes and etc.) into macroscopic configuration for more possible practical application.

METHODS

Materials

Graphene sheets with the average lateral size of 5.4 ± 0.3 μm and thickness of 10.6 ± 0.3 nm were prepared through the intercalation and exfoliation of graphite. Porous PU film was obtained from Suzhou Shutao Medical Supplies Co., Ltd. (China). The epoxy matrix (6105) and the hardener (methyl-hexahydrophthalic anhydride, MHHPA) were purchased from DOW Chemicals (USA) and Shanghai Li Yi Science & Technology Development Co. Ltd. (China), respectively. The Neodymium(III) acetylacetonate trihydrate (Nd(III)acac) was purchased from Aldrich Chemicals. Polyethylene glycol (PEG) with the numerical-molecular average weight (Mn) of 4000 was purchased from Aladdin Reagent Co., Ltd. Polydimethylsiloxane (PDMS, Sylgard 184) and the hardener were purchased from Dow Corning Co., Ltd. (Shanghai, China). Ethanol was purchased from Sinopharm Chemical Reagent Co., Ltd. (China). All chemicals were of analytical reagent grade and used without further purification.

Preparation of the DAGF

Graphene/PU monolith was prepared using a dual-assembly strategy, by which porous PU film was continuously immersed in graphene/ethanol solution (10 mg/ml) to assemble graphene sheets on the surface of PU skeleton, followed by a continuous roll-to-roll step to roll up the film into a cylinder. The film was kept in a tensile state in the roll-to-roll process and the stretch ratio was strictly controlled and ranged from 0 to 340%. Then, as-prepared graphene/PU monolith was thermally annealed at 1000 °C (1 h) in vacuum for the removal of the PU, followed by the graphitization at 2850 °C (2 h) in argon atmosphere to obtain a series of DAGF (DAGF1 – 5).

Preparation of the DAGF/EP composites

Initially, Nd(III)acac was added into epoxy precursor and stirred for 2 h (80 °C) to prepare a

homogeneous solution, which was subsequently mixed with curing agent (MHHPA) at the weight ratio of 100 : 95 to obtain the epoxy prepolymer. Then, a series of DAGF (DAGF1 – 5) was immersed into the prepolymer for 1 h under vacuum to infiltrate epoxy and remove the air bubbles. Finally, a procedural thermal curing of 135°C (2 h) and 165 °C (14 h) was carried out to obtain the DAGF/EP composites (DAGF1/EP – DAGF5/EP).

Preparation of the DAGF5/PEG and DAGF5/PDMS composites

The DAGF5/PEG composites were fabricated by the infiltration of PEG into porous DAGF5 framework with the assistance of vacuum. The raw PEG powder was first heated to 90 °C to obtain a fully melted PEG with a good fluidity. Then, the DAGF5 framework was immersed into the melted PEG, and moved the both in a vacuum oven at 90 °C for 5 h to fully infiltrate the PEG and remove the air bubbles. Finally, the sample was cooled at room temperature to obtain the DAGF5/PEG composite. The DAGF5/PEG composites were prepared by the immersion of the DAGF5 framework into the mixture of PDMS prepolymer and curing agent with the weight ratio of 50:1. Then the sample was placed in a vacuum oven more than 4 h (room temperature) to remove the air bubbles, followed by curing at 80 °C for 5 h to obtained the DAGF5/PDMS composites.

Characterizations

Raman spectra were recorded using a Reflex Raman System (Renishaw plc, Wotton-under-edge, UK) employing a laser wavelength of 532 nm. The sample morphologies were examined with field emission scanning electron microscopy (FE-SEM, Quanta FEG250, FEI, USA). Thermogravimetric analysis (TGA) was performed using a PYRIS Diamond^{TM} system (PerkinElmer, USA) to confirm the weight percent of graphene in the polymer matrix. The measurements were carried out under nitrogen in the range from 30 to 800 ^{o}C at the heating rate of 20 ^{o}C/min. The thermal diffusivities (α)

of the sample were measured using LFA 467 MicroFlash$^{®}$ system (NETZSCH, Germany). The

thermal conductivity (κ) can be calculated by the equation: $\kappa = \alpha \times \rho \times C_p$, where ρ is the measured

average density determined by the water displacement method and C_p is specific heat capacity of the

sample evaluated by using a differential scanning calorimeter (DSC) (PYRIS Diamond^{TM},

PerkinElmer, USA). The infrared (IR) photos were captured by using an infrared camera (Fluke,

Ti400, USA).

ASSOCIATED CONTENT

Supporting Information

The Supporting Information is available free of charge on the ACS Publications website at DOI:

The analysis of the thermal conductivity for the DAGF/EP composites using the metal foam theory.

The analysis of the thermal conductivity for the DAGF/EP composites according to the Foygel

nonlinear model. Raman spectra and XRD patterns of the pristine graphene/PU and DAGF.

Cross-sectional SEM image of the applied porous PU film. Schematic and TGA analysis of CG/PU

and DAG/PU at different sampling regions. TGA curves of neat epoxy and DAGF/EP composites in

nitrogen atmosphere. Schematic of the NEMD implementation and the results of the junction thermal

conductance for the adjacent graphene sheets with different overlapping area. DSC heating scan

curves of pure PEG and DAGF5/PEG with the heating rate changing from 10 to 90 °C min^{-1}.

Schematic of the ANSYS simulation models the results of the transient thermal response for the neat

PEG and DAGF5/PEG. Schematic illustrating the solar-thermal energy conversion measurement of

neat PEG and DAGF5/PEG. Icepak system model and the corresponding results for TIM

performance evaluation of DAGF5/PDMS. The parameters for the calculation of in-plane and

through-plane thermal conductivity of neat epoxy and the DAGF/EP composites. Comparison of thermal conductivity of our DAGF/polymer composites with reported graphene/polymer composites. The parameters obtained from the Foygel model, and the calculated overlapping area of adjacent graphene sheets. A comparison of the thermal conductivity and the thermal effusivity of our DAGF5/PEG and with reported carbon-based phase-change composites. The detailed parameters for the Icepak simulation implementation. The calculated total thermal resistance and contact thermal resistance of the applied TIMs.

AUTHOR INFORMATION

Corresponding Author

*E-mail: jiangnan@nimte.ac.cn.

*E-mail: linzhengde@nimte.ac.cn.

ORCID

Wen Dai: 0000-0003-0601-5150

Jinhong Yu: 0000-0001-9134-7568

Rong Sun: 0000-0001-9719-3563

Ching-Ping Wong: 0000-0003-3556-8053

Cheng-Te Lin: 0000-0002-7090-9610

Author Contributions

REFERENCES

1. Moore, A. L.; Shi, L., Emerging challenges and materials for thermal management of electronics. *Materials Today* **2014,** *17* (4), 163-174.

2. Waldrop, M. M., The chips are down for Moore's law. *Nature News* **2016,** *530* (7589), 144.

3. Li, S.; Zheng, Q.; Lv, Y.; Liu, X.; Wang, X.; Huang, P. Y.; Cahill, D. G.; Lv, B., High thermal conductivity in cubic boron arsenide crystals. *Science* **2018,** *361* (6402), 579-581.

4. Schelling, P. K.; Shi, L.; Goodson, K. E., Managing heat for electronics. *Materials Today* **2005,** *8* (6), 30-35.

5. Pop, E.; Sinha, S.; Goodson, K. E., Heat Generation and Transport in Nanometer-Scale Transistors. *Proceedings of the IEEE* **2006,** *94* (8), 1587-1601.

6. Razeeb, K. M.; Dalton, E.; Cross, G. L. W.; Robinson, A. J., Present and future thermal interface materials for electronic devices. *International Materials Reviews* **2018,** *63* (1), 1-21.

7. Hansson, J.; Nilsson, T. M.; Ye, L.; Liu, J., Novel nanostructured thermal interface materials: a review. *International Materials Reviews* **2018,** *63* (1), 22-45.

8. Giri, A.; Hopkins, P. E., A review of experimental and computational advances in thermal boundary conductance and nanoscale thermal transport across solid interfaces. *Advanced Functional Materials* **2020,** *30* (8), 1903857.

9. Min, P.; Liu, J.; Li, X.; An, F.; Liu, P.; Shen, Y.; Koratkar, N.; Yu, Z. Z., Thermally Conductive Phase Change Composites Featuring Anisotropic Graphene Aerogels for Real-Time and Fast-Charging Solar-Thermal Energy Conversion. Advanced Functional Materials 2018, 28 (51), 1805365.

10. Yuan, K.; Shi, J.; Aftab, W.; Qin, M.; Usman, A.; Zhou, F.; Lv, Y.; Gao, S.; Zou, R., Engineering the Thermal Conductivity of Functional Phase-Change Materials for Heat Energy Conversion, Storage, and Utilization. Advanced Functional Materials 2020, 30 (8), 1904228.

11. Balandin, A. A.; Ghosh, S.; Bao, W.; Calizo, I.; Teweldebrhan, D.; Miao, F.; Lau, C. N., Superior thermal conductivity of single-layer graphene. *Nano letters* **2008,** *8* (3), 902-907.

12. Xu, X.; Pereira, L. F.; Wang, Y.; Wu, J.; Zhang, K.; Zhao, X.; Bae, S.; Bui, C. T.; Xie, R.; Thong, J. T., Length-dependent thermal conductivity in suspended single-layer graphene. *Nature communications* **2014,** *5* (1), 1-6.

13. Peng, L.; Xu, Z.; Liu, Z.; Guo, Y.; Li, P.; Gao, C., Ultrahigh thermal conductive yet superflexible graphene films. *Advanced Materials* **2017,** *29* (27), 1700589.

14. Xin, G.; Sun, H.; Hu, T.; Fard, H. R.; Sun, X.; Koratkar, N.; Borca-Tasciuc, T.; Lian, J., Large-area freestanding graphene paper for superior thermal management. *Advanced materials* **2014,** *26* (26), 4521-4526.

15. Renteria, J. D.; Ramirez, S.; Malekpour, H.; Alonso, B.; Centeno, A.; Zurutuza, A.; Cocemasov, A. I.; Nika, D. L.; Balandin, A. A., Strongly anisotropic thermal conductivity of free-standing reduced graphene oxide films annealed at high temperature. Advanced Functional Materials 2015, 25 (29), 4664-4672.

16. Ren, H.; Tang, M.; Guan, B.; Wang, K.; Yang, J.; Wang, F.; Wang, M.; Shan, J.; Chen, Z.; Wei, D., Hierarchical graphene foam for efficient omnidirectional solar–thermal energy conversion. *Advanced Materials* **2017,** *29* (38), 1702590.

17. Zhang, P.; Li, J.; Lv, L.; Zhao, Y.; Qu, L., Vertically aligned graphene sheets membrane for highly efficient solar thermal generation of clean water. *ACS nano* **2017,** *11* (5), 5087-5093.

18. Ergoktas, M. S.; Bakan, G.; Steiner, P.; Bartlam, C.; Malevich, Y.; Yenigun, E. O.; He, G.; Karim, N.; Cataldi, P.; Bissett, M., Graphene-enabled adaptive infrared textiles. *arXiv preprint arXiv:2004.08629* **2020**.

19. Shen, X.; Wang, Z.; Wu, Y.; Liu, X.; He, Y.-B.; Zheng, Q.; Yang, Q.-H.; Kang, F.; Kim, J.-K., A three-dimensional multilayer graphene web for polymer nanocomposites with exceptional transport properties and fracture resistance. *Materials Horizons* **2018,** *5* (2), 275-284.

20. Shen, X.; Wang, Z.; Wu, Y.; Liu, X.; He, Y.-B.; Kim, J.-K., Multilayer graphene enables higher efficiency in improving thermal conductivities of graphene/epoxy composites. *Nano letters* **2016,** *16* (6), 3585-3593.

21. Lian, G.; Tuan, C.-C.; Li, L.; Jiao, S.; Wang, Q.; Moon, K.-S.; Cui, D.; Wong, C.-P., Vertically aligned and interconnected graphene networks for high thermal conductivity of epoxy composites with ultralow loading. *Chemistry of Materials* **2016,** *28* (17), 6096-6104.

22. Wu, Z.; Xu, C.; Ma, C.; Liu, Z.; Cheng, H. M.; Ren, W., Synergistic effect of aligned graphene nanosheets in graphene foam for high‑performance thermally conductive composites. Advanced Materials 2019, 31 (19), 1900199.

23. Wu, S.; Li, T.; Tong, Z.; Chao, J.; Zhai, T.; Xu, J.; Yan, T.; Wu, M.; Xu, Z.; Bao, H., High-Performance Thermally Conductive Phase Change Composites by Large-Size Oriented Graphite Sheets for Scalable Thermal Energy Harvesting. Advanced Materials 2019, 31 (49), 1905099.

24. Shtein, M.; Nadiv, R.; Buzaglo, M.; Kahil, K.; Regev, O., Thermally conductive graphene-polymer composites: size, percolation, and synergy effects. *Chemistry of Materials* **2015,** *27* (6), 2100-2106.

25. Song, S. H.; Park, K. H.; Kim, B. H.; Choi, Y. W.; Jun, G. H.; Lee, D. J.; Kong, B. S.; Paik, K. W.; Jeon, S., Enhanced thermal conductivity of epoxy–graphene composites by using non-oxidized graphene flakes with non-covalent functionalization. Advanced Materials 2013, 25 (5), 732-737.

26. Alam, F. E.; Dai, W.; Yang, M.; Du, S.; Li, X.; Yu, J.; Jiang, N.; Lin, C.-T., In situ formation of a cellular graphene framework in thermoplastic composites leading to superior thermal conductivity. *Journal of Materials Chemistry A* **2017,** *5* (13), 6164-6169.

27. Shahil, K. M.; Balandin, A. A., Graphene–multilayer graphene nanocomposites as highly efficient thermal interface materials. *Nano letters* **2012,** *12* (2), 861-867.

28. Ganguli, S.; Roy, A. K.; Anderson, D. P., Improved thermal conductivity for chemically functionalized exfoliated graphite/epoxy composites. *Carbon* **2008,** *46* (5), 806-817.

29. Yu, A.; Ramesh, P.; Sun, X.; Bekyarova, E.; Itkis, M. E.; Haddon, R. C., Enhanced thermal conductivity in a hybrid graphite nanoplatelet–carbon nanotube filler for epoxy composites. *Advanced Materials* **2008,** *20* (24), 4740-4744.

30. Teng, C.-C.; Ma, C.-C. M.; Lu, C.-H.; Yang, S.-Y.; Lee, S.-H.; Hsiao, M.-C.; Yen, M.-Y.; Chiou, K.-C.; Lee, T.-M., Thermal conductivity and structure of non-covalent functionalized graphene/epoxy composites. *Carbon* **2011,** *49* (15), 5107-5116.

31. Hou, H.; Dai, W.; Yan, Q.; Lv, L.; Alam, F. E.; Yang, M.; Yao, Y.; Zeng, X.; Xu, J.-B.; Yu, J., Graphene size-dependent modulation of graphene frameworks contributing to the superior thermal conductivity of epoxy composites. *Journal of Materials Chemistry A* **2018,** *6* (25), 12091-12097.

32. Yang, J.; Li, X.; Han, S.; Yang, R.; Min, P.; Yu, Z.-Z., High-quality graphene aerogels for thermally conductive phase change composites with excellent shape stability. *Journal of Materials Chemistry A* **2018,** *6* (14), 5880-5886.

33. Ji, H.; Sellan, D. P.; Pettes, M. T.; Kong, X.; Ji, J.; Shi, L.; Ruoff, R. S., Enhanced thermal conductivity of phase change materials with ultrathin-graphite foams for thermal energy storage. *Energy & Environmental Science* **2014,** *7* (3), 1185-1192.

34. Zhan, H.; Nie, Y.; Chen, Y.; Bell, J. M.; Gu, Y., Thermal transport in 3D nanostructures. *Advanced Functional Materials* **2020,** *30* (8), 1903841.

35. Balandin, A. A., Thermal properties of graphene and nanostructured carbon materials. *Nature materials* **2011,** *10* (8), 569-581.

36. Cai, W.; Moore, A. L.; Zhu, Y.; Li, X.; Chen, S.; Shi, L.; Ruoff, R. S., Thermal transport in suspended and supported monolayer graphene grown by chemical vapor deposition. *Nano letters* **2010,** *10* (5), 1645-1651.

37. Wang, C.; Chen, X.; Wang, B.; Huang, M.; Wang, B.; Jiang, Y.; Ruoff, R. S., Freeze-casting produces a

graphene oxide aerogel with a radial and centrosymmetric structure. *ACS nano* **2018,** *12* (6), 5816-5825.

38. Zhao, N.; Yang, M.; Zhao, Q.; Gao, W.; Xie, T.; Bai, H., Superstretchable nacre-mimetic graphene/poly (vinyl alcohol) composite film based on interfacial architectural engineering. *ACS nano* **2017,** *11* (5), 4777-4784.

39. Xu, Z.; Gao, C., Aqueous liquid crystals of graphene oxide. *Acs Nano* **2011,** *5* (4), 2908-2915.

40. Narayan, R.; Kim, J. E.; Kim, J. Y.; Lee, K. E.; Kim, S. O., Graphene oxide liquid crystals: discovery, evolution and applications. *Advanced Materials* **2016,** *28* (16), 3045-3068.

41. Qiu, L.; Liu, J. Z.; Chang, S. L.; Wu, Y.; Li, D., Biomimetic superelastic graphene-based cellular monoliths. *Nature communications* **2012,** *3* (1), 1-7.

42. Li, X.-H.; Liu, P.; Li, X.; An, F.; Min, P.; Liao, K.-N.; Yu, Z.-Z., Vertically aligned, ultralight and highly compressive all-graphitized graphene aerogels for highly thermally conductive polymer composites. *Carbon* **2018,** *140*, 624-633.

43. Guo, F.; Shen, X.; Zhou, J.; Liu, D.; Zheng, Q.; Yang, J.; Jia, B.; Lau, A. K.; Kim, J. K., Highly Thermally Conductive Dielectric Nanocomposites with Synergistic Alignments of Graphene and Boron Nitride Nanosheets. *Advanced Functional Materials* **2020,** *30* (19), 1910826.

44. Kim, J. E.; Han, T. H.; Lee, S. H.; Kim, J. Y.; Ahn, C. W.; Yun, J. M.; Kim, S. O., Graphene oxide liquid crystals. *Angewandte Chemie* **2011,** *123* (13), 3099-3103.

45. Yao, B.; Chen, J.; Huang, L.; Zhou, Q.; Shi, G., Base-Induced Liquid Crystals of Graphene Oxide for Preparing Elastic Graphene Foams with Long-Range Ordered Microstructures. Advanced Materials 2016, 28 (8), 1623-1629.

46. An, F.; Li, X.; Min, P.; Liu, P.; Jiang, Z.-G.; Yu, Z.-Z., Vertically aligned high-quality graphene foams for anisotropically conductive polymer composites with ultrahigh through-plane thermal conductivities. *ACS applied materials & interfaces* **2018,** *10* (20), 17383-17392.

47. Li, Y.; Wei, W.; Wang, Y.; Kadhim, N.; Mei, Y.; Zhou, Z., Construction of highly aligned graphene-based aerogels and their epoxy composites towards high thermal conductivity. *Journal of Materials Chemistry C* **2019,** *7* (38), 11783-11789.

48. Yang, Z. Y.; Jin, L. J.; Lu, G. Q.; Xiao, Q. Q.; Zhang, Y. X.; Jing, L.; Zhang, X. X.; Yan, Y. M.; Sun, K. N., Sponge-templated preparation of high surface area graphene with ultrahigh capacitive deionization performance. Advanced Functional Materials 2014, 24 (25), 3917-3925.

49. Li, B.; Yang, S.; Li, S.; Wang, B.; Liu, J., From commercial sponge toward 3D graphene–silicon networks for superior lithium storage. Advanced Energy Materials 2015, 5 (15), 1500289.

50. Niu, Z.; Zhou, W.; Chen, X.; Chen, J.; Xie, S., Highly compressible and all-solid-state supercapacitors based on nanostructured composite sponge. Advanced materials 2015, 27 (39), 6002-6008.

51. Xu, J.; Tan, Z.; Zeng, W.; Chen, G.; Wu, S.; Zhao, Y.; Ni, K.; Tao, Z.; Ikram, M.; Ji, H., A hierarchical carbon derived from sponge-templated activation of graphene oxide for high-performance supercapacitor electrodes. Advanced Materials 2016, 28 (26), 5222-5228.

52. Li, X.; Chen, Y.; Kumar, A.; Mahmoud, A.; Nychka, J. A.; Chung, H.-J., Sponge-templated macroporous graphene network for piezoelectric ZnO nanogenerator. *ACS applied materials & interfaces* **2015,** *7* (37),

20753-20760.

53. Kholmanov, I.; Kim, J.; Ou, E.; Ruoff, R. S.; Shi, L., Continuous carbon nanotube–ultrathin graphite hybrid foams for increased thermal conductivity and suppressed subcooling in composite phase change materials. *ACS nano* **2015,** *9* (12), 11699-11707.

54. Dai, W.; Yu, J.; Wang, Y.; Song, Y.; Alam, F. E.; Nishimura, K.; Lin, C.-T.; Jiang, N., Enhanced thermal conductivity for polyimide composites with a three-dimensional silicon carbide nanowire@ graphene sheets filler. *Journal of Materials Chemistry A* **2015,** *3* (9), 4884-4891.

55. Li, Q.; Guo, Y.; Li, W.; Qiu, S.; Zhu, C.; Wei, X.; Chen, M.; Liu, C.; Liao, S.; Gong, Y., Ultrahigh thermal conductivity of assembled aligned multilayer graphene/epoxy composite. *Chemistry of Materials* **2014,** *26* (15), 4459-4465.

56. Jung, H.; Yu, S.; Bae, N.-S.; Cho, S. M.; Kim, R. H.; Cho, S. H.; Hwang, I.; Jeong, B.; Ryu, J. S.; Hwang, J., High through-plane thermal conduction of graphene nanoflake filled polymer composites melt-processed in an L-shape kinked tube. *ACS applied materials & interfaces* **2015,** *7* (28), 15256-15262.

57. An, F.; Li, X.; Min, P.; Li, H.; Dai, Z.; Yu, Z.-Z., Highly anisotropic graphene/boron nitride hybrid aerogels with long-range ordered architecture and moderate density for highly thermally conductive composites. *Carbon* **2018,** *126*, 119-127.

58. Barani, Z.; Mohammadzadeh, A.; Geremew, A.; Huang, C. Y.; Coleman, D.; Mangolini, L.; Kargar, F.; Balandin, A. A., Thermal properties of the binary-filler hybrid composites with graphene and copper nanoparticles. Advanced Functional Materials 2020, 30 (8), 1904008.

59. Foygel, M.; Morris, R.; Anez, D.; French, S.; Sobolev, V., Theoretical and computational studies of carbon nanotube composites and suspensions: Electrical and thermal conductivity. *Physical Review B* **2005,** *71* (10), 104201.

60. Zeng, X.; Yao, Y.; Gong, Z.; Wang, F.; Sun, R.; Xu, J.; Wong, C. P., Ice-templated assembly strategy to construct 3D boron nitride nanosheet networks in polymer composites for thermal conductivity improvement. *Small* **2015,** *11* (46), 6205-6213.

61. Hu, J.; Huang, Y.; Yao, Y.; Pan, G.; Sun, J.; Zeng, X.; Sun, R.; Xu, J.-B.; Song, B.; Wong, C.-P., Polymer composite with improved thermal conductivity by constructing a hierarchically ordered three-dimensional interconnected network of BN. *ACS applied materials & interfaces* **2017,** *9* (15), 13544-13553.

62. Wei, Y.; Li, J.; Sun, F.; Wu, J.; Zhao, L., Leakage-proof phase change composites supported by biomass carbon aerogels from succulents. *Green Chemistry* **2018,** *20* (8), 1858-1865.

63. Cottrill, A. L.; Liu, A. T.; Kunai, Y.; Koman, V. B.; Kaplan, A.; Mahajan, S. G.; Liu, P.; Toland, A. R.; Strano, M. S., Ultra-high thermal effusivity materials for resonant ambient thermal energy harvesting. *Nature communications* **2018,** *9* (1), 1-11.

64. Yuan, K.; Liu, J.; Fang, X.; Zhang, Z., Novel facile self-assembly approach to construct graphene oxide-decorated phase-change microcapsules with enhanced photo-to-thermal conversion performance.

Journal of Materials Chemistry A **2018,** *6* (10), 4535-4543.

65. Wang, M.; Zhang, T.; Mao, D.; Yao, Y.; Zeng, X.; Ren, L.; Cai, Q.; Mateti, S.; Li, L. H.; Zeng, X., Highly compressive boron nitride nanotube aerogels reinforced with reduced graphene oxide. *ACS nano* **2019,** *13* (7), 7402-7409.

66. Yang, J.; Li, X.; Han, S.; Zhang, Y.; Min, P.; Koratkar, N.; Yu, Z.-Z., Air-dried, high-density graphene hybrid aerogels for phase change composites with exceptional thermal conductivity and shape stability. *Journal of Materials Chemistry A* **2016,** *4* (46), 18067-18074.

67. Yang, J.; Qi, G.-Q.; Bao, R.-Y.; Yi, K.; Li, M.; Peng, L.; Cai, Z.; Yang, M.-B.; Wei, D.; Yang, W., Hybridizing graphene aerogel into three-dimensional graphene foam for high-performance composite phase change materials. *Energy Storage Materials* **2018,** *13*, 88-95.

68. Yang, J.; Zhang, E.; Li, X.; Zhang, Y.; Qu, J.; Yu, Z.-Z., Cellulose/graphene aerogel supported phase change composites with high thermal conductivity and good shape stability for thermal energy storage. *Carbon* **2016,** *98*, 50-57.

69. Wu, H.-y.; Li, S.-t.; Shao, Y.-w.; Jin, X.-z.; Qi, X.-d.; Yang, J.-h.; Zhou, Z.-w.; Wang, Y., Melamine foam/reduced graphene oxide supported form-stable phase change materials with simultaneous shape memory property and light-to-thermal energy storage capability. *Chemical Engineering Journal* **2020,** *379*, 122373.

70. Xue, F.; Lu, Y.; Qi, X.-d.; Yang, J.-h.; Wang, Y., Melamine foam-templated graphene nanoplatelet framework toward phase change materials with multiple energy conversion abilities. *Chemical Engineering Journal* **2019,** *365*, 20-29.

71. Chen, X.; Gao, H.; Yang, M.; Dong, W.; Huang, X.; Li, A.; Dong, C.; Wang, G., Highly graphitized 3D network carbon for shape-stabilized composite PCMs with superior thermal energy harvesting. *Nano energy* **2018,** *49*, 86-94.

72. Dai, W.; Ma, T.; Yan, Q.; Gao, J.; Tan, X.; Lv, L.; Hou, H.; Wei, Q.; Yu, J.; Wu, J., Metal-level thermally conductive yet soft graphene thermal interface materials. *ACS nano* **2019,** *13* (10), 11561-11571.

73. Dai, W.; Lv, L.; Lu, J.; Hou, H.; Yan, Q.; Alam, F. E.; Li, Y.; Zeng, X.; Yu, J.; Wei, Q., A paper-like inorganic thermal interface material composed of hierarchically structured graphene/silicon carbide nanorods. *ACS nano* **2019,** *13* (2), 1547-1554.

74. Hallam, C.; Griffiths, W., A model of the interfacial heat-transfer coefficient for the aluminum gravity die-casting process. *Metallurgical and materials transactions B* **2004,** *35* (4), 721-733.